Open Access

Research Article

Lego-Microfluidics Generated Magnetically Responsive Bifunctional Microcapsules with Encapsulated Phase Change Material

Sumit Parvate, Seyedarash Moshtaghibana, Madhav Solanke, Nibina Nizar, Nico Leister, Philipp Schochat, Kelly Morrison, Sujay Chattopadhyay, and Goran T. Vladisavljević*

Cite This: ACS Sustainable Chem. Eng. 2024, 12, 6389−6399

Read Online

ACCESS | Metrics & More | Article Recommendations | Supporting Information

ABSTRACT: We report an innovative Lego-microfluidic technology for room temperature synthesis of highly monodispersed bifunctional microcapsules enclosing phase change material (PCM), exhibiting magnetic and thermal energy storage properties. Iron(II, III) oxide (Fe_3O_4) nanoparticle-embedded microcapsules encapsulating hexadecane (HD) are synthesized without external heating or cooling in just ∼80 s. The process involves forming oil-in-oil-in-water (O/O/W) double emulsion droplets with Norland Optical Adhesive (NOA) photopolymeric shell and consolidating them through on-the-fly shell polymerization using thiol−ene "click" chemistry. PCM content and magnetic properties were accurately manipulated by adjusting inner phase (PCM) flow rate and mass fraction of Fe_3O_4 nanoparticles in the middle (polymer) phase. Microcapsules with a shell thickness of 17.1 μm achieved a maximum PCM content of 63.3%. Thermogravimetric analysis (TGA) revealed significantly enhanced thermal stability of Fe_3O_4 nanoparticle-embedded microcapsules compared to pure PCM. Vibrating sample magnetometry (VSM) verified an increase in saturation magnetization and residual magnetization of microcapsules, having higher Fe_3O_4 nanoparticle content. Notably, the sample containing 1% Fe_3O_4 nanoparticles exhibited excellent magnetic properties, showcasing a saturation magnetization of 0.194 emu/g. Concurrently, the PCM microcapsules demonstrated high magnetic responsiveness and maneuverability.

KEYWORDS: phase change material, microfluidics, microencapsulation, microcapsules, magnetoresponsive, thermal energy storage
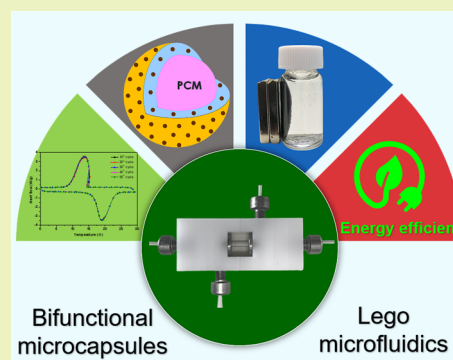
1. INTRODUCTION

Thermal energy storage utilizing latent heat is regarded as an elegant and feasible solution for addressing environmental crises and reducing dependence on fossil fuels. Phase change materials (PCMs) are novel renewable energy storage materials that have gained significant attention due to their impressive capacity to store and release latent heat, phase transitions at constant temperatures, excellent thermal stability, and minimal volume variations during phase change.[1] Despite such advantages, PCMs have inherent problems such as leakage during melting, low thermal conductivity, corrosiveness, and supercooling tendency, which present significant obstacles to their direct implementation in practical settings.[2] To address these issues, microencapsulation has emerged as a prominent strategy involving the formation of core−shell structures composed of tiny droplets of PCMs encapsulated within a film-forming material.[3] This approach effectively addresses the aforementioned challenges related to PCMs and enables applications of PCMs in diverse fields like construction materials, medicine, food packaging, thermo-regulated textiles, waste energy recovery, and electronics.[3−5] Particularly, PCM microcapsules with magnetic properties are being explored in various applications, including magnetically driven microrobots with thermal energy storage capability,[6] PCMs with modular

assembly and geometric conformality features,[7] and infrared electromagnetic double shielding in electronic gadgets and military electronics.[8] Zhuang et al.[9] developed magnetic PCM microcapsules with Fe_3O_4 decorated acrylic copolymer shell and octadecane core using suspension polymerization. Jiang et al.[10] synthesized magnetic PCM microcapsules using a Fe_3O_4/SiO_2 hybrid shell with an n-eicosane core using interfacial polycondensation technique. Similarly, various synthesis methods, including interfacial polymerization, emulsion polymerization, Pickering emulsion polymerization, complex coacervation, in situ polymerization, self-assembly, and sol−gel techniques, have been documented for the synthesis of multifunctional microcapsules.[11] However, these encapsulation methods rely on traditional top-down emulsification approaches that involve emulsifying machines such as ultrasonic and high-pressure homogenizers and rotor-stator devices.[12] These techniques, where larger droplets are broken into
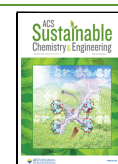
Table 1. Process Conditions for the Preparation of Microcapsule Samples

| sample | Fe_3O_4 concentration in middle phase (wt %) | flow rate of phase (mL/h) | | | capillary tip inner diameter (μm) | |
		inner (Q_i)	middle (Q_m)	outer (Q_o)	injection (D_{ii})	collection (D_{ci})
MC1	1.0	0.5	1.0	20	100	400
MC2	1.0	1.0	1.0	20	100	400
MC3	1.0	2.0	1.0	20	100	400
MC4	0.2	2.0	1.0	20	100	400
MC5	0.6	2.0	1.0	20	100	400

smaller droplets, require high amounts of energy and result in low encapsulation yields. Moreover, the subsequent droplets exhibit a high degree of size variation, making it difficult to control the subsequent capsule structure and functionality. The particle size distribution obtained through these traditional methods lacks reproducibility, restricting the potential applications of these techniques.[13] Importantly, these techniques necessitate surface modification of nanoparticles either to make them compatible with the polymeric shell material or to stabilize the emulsion.[14,15] Such additional steps can potentially compromise their inherent functionality. Furthermore, traditional encapsulation processes are often time-consuming and involve multiple stages, with reaction times lasting approximately 24 h.[16]

Droplet microfluidics offers a promising approach to overcoming the challenges of bulk emulsification by producing microcapsules with precisely defined morphology. The glass capillary-based microfluidic devices were first developed in Weitz's lab at Harvard University.[17] Based on the success of capillary microfluidics, Lone et al.[18] developed tubular microfluidics to encapsulate octadecane within a polyurea shell. Building on this progress, Fu et al.[19] utilized a coflow microfluidic device with three coaxial cylindrical glass capillaries to fabricate elastic microcapsules with silicone shells and a core of *n*-hexadecyl bromide. The progress in microfluidic-based encapsulation of PCMs has been recently reviewed by Guo et al.[20] These advances highlight the exceptional potential of droplet microfluidics in precise and controlled microencapsulation processes.

However, the fabrication of existing microfluidic devices is challenging and time-consuming. Capillaries in a conventional disposable glass capillary device are firmly secured to a glass microscope slide with epoxy glue, making it impossible to readjust their position during droplet generation.[21] This limitation hinders customization and fine adjustment of microcapsule structure. Furthermore, the fabrication process of conventional glass capillary devices is so complicated that even a slight misalignment or positioning error in the capillaries makes the entire apparatus nonfunctional. Conversely, the fabrication of PDMS channels depends on expensive photolithographically defined master molds. These factors contribute to the overall high cost and complexity of manufacturing PDMS-based microfluidic devices.[22]

We report an innovative Lego-inspired glass capillary microfluidic device to prepare Fe_3O_4-embedded PCM microcapsules through on-the-fly UV polymerization. This process is highly energy efficient (requiring no heating or cooling), environmentally friendly, reproducible, and rapid (capsule solidification time ~80 s). The Lego device consists of glass capillaries inserted in two CNC-milled blocks that can be interconnected and disassembled using a stud-and-tube system inspired by Lego. Since screws fix the capillaries, they can be moved during droplet generation for *in situ* optimization of

their position and alignment. Norland Optical Adhesive (NOA), a nonacrylate photopolymer that cures through thiol−ene "click" reactions was used as a capsule shell material. This choice was driven by the strict environmental and safety regulations for acrylates and amino resins such as urea−formaldehyde and melamine−formaldehyde.[12] Organic PCM, i.e., hexadecane (HD) was used as a PCM due to its substantial melting enthalpy of ~240 J/g at the phase transition temperature of ~20 °C. The choice to embed Fe_3O_4 nanoparticles into the PCM microcapsules was driven by their outstanding magnetic properties, derived from their inherent ferrimagnetism. This energy-efficient synthesis led to the formation of bifunctional PCM microcapsules with simultaneous heat energy storage capability and magnetic responsiveness.

2. EXPERIMENTAL SECTION

2.1. Materials. The synthesis technique involved the use of Norland Optical Adhesive (NOA81, Norland Products, New Jersey) as the shell material. NOA is a UV-curable thiol−ene polymer that contains triallyl isocyanurate and mercapto-ester with a viscosity of 300 mPa·s at 25 °C.[23,24] Due to high viscosity of NOA, nanoparticles were dispersed in an 80:20 mixture by mass of NOA and acetone with a viscosity of 0.0119 Pa·s and a density of 1176 kg/m³. The suspension of iron(II, III) oxide (Fe_3O_4) nanoparticles (Sigma-Aldrich) in the NOA−acetone mixture was used as the middle phase. Hexadecane (HD, 99% purity, Sigma-Aldrich) with a viscosity of 0.0033 Pa·s and a density of 773 kg/m³ was chosen as the organic PCM (the core material or inner phase). The equilibrium interfacial tension was 6.3, 9.2, and 49.8 mN/m at the inner/middle phase, middle/outer phase, and inner/outer phase interface, respectively. The outer phase comprised an aqueous mixture of 2 wt % poly(vinyl alcohol) (PVA 31,000−50,000 mol/g, Alfa Aesar) and 30 wt % glycerol (Sigma-Aldrich) with a viscosity of 0.0047 Pa·s and a density of 1078 kg/m³. Here, glycerol was added to control the viscosity of the outer phase, while PVA served as a stabilizing agent for the double emulsion droplets. The experimental conditions used to prepare the samples of PCM microcapsules are shown in Table 1.

2.2. Equipment and Procedure. Borosilicate round capillaries acquired from World Precision Instruments, UK were used in the microfluidic device. The outer capillary had an inner diameter/outer diameter of 1.56/2.0 mm, while the diameters of the inner capillary were 0.58/1.0 mm. An inner capillary tube was pulled from its center region using a P-97 micropipette puller (Sutter Instruments, USA) and divided into two separate capillaries: the injection capillary and the collection capillary. The tips of both capillaries were trimmed by grazing over sandpaper to achieve the desired orifice diameter and measured using the MF-830 Microforge microscope.
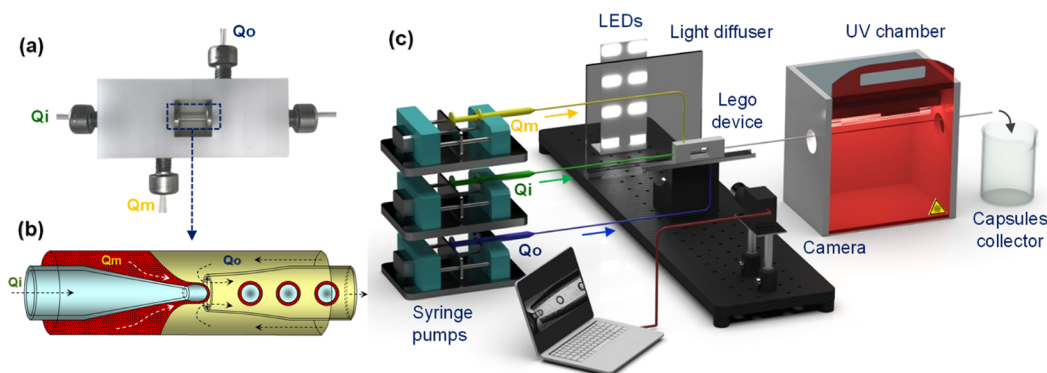
Figure 1. (a) Schematic illustration of the Lego microfluidic device (Q_i — inner PCM phase, Q_m — middle NOA + acetone phase, and Q_o — outer PVA solution + glycerol phase); (b) microfluidic process of core−shell droplet formation; (c) experimental setup.

The SolidWorks program by Dassault Systèmes was used to create a 3D design of two interlocking polyacetal Lego blocks (density of 1410 kg/m^3). An automated Computer Numerical Control (CNC) milling machine (HAAS Automation, UK) was employed for the block fabrication. The 3D design and photograph of the Lego blocks are shown in Figures S1 and S2.

A custom-designed reconfigurable rig was assembled to facilitate the smooth and efficient synthesis of microcapsules (Figures 1c and S3). The Lego device was set on a holder attached to a linear translation platform, allowing precise movement via a micrometer to ensure that the interior of the device can be brought into perfect focus. The droplet production process was captured using a monochrome camera (The Imaging Source DMK 33UX287) outfitted with a TMN 1.0/50 lens (1×). A light-emitting diode (LED) panel comprising 48 LED lights (12 V) along with a light-diffusing acrylic sheet was fixed behind the device to capture high-resolution images. Notably, custom-made metal connections attached to polyethylene tubing (ID/OD 0.86/1.52 mm, Smiths Medical, UK) were used to seal the injection and collection inlets (Figure S2). Furthermore, the inner capillaries were firmly secured in their designated blocks by attaching metal connectors with O-rings at the injection and collection inlets. Syringe pumps (Harvard Apparatus, UK) were used to pump liquid phases out of gastight 10 mL, 25 mL, and 50 mL SGE glass syringes. The IC Capture software (Imaging Source, Germany) was used to record the entire microfluidic process.[25] The ImageJ program (National Institutes of Health) was then used for particle size analysis and video edits.

A counter-current flow focusing technique was implemented to generate core−shell droplets, which involved utilizing a coaxial jet composed of PCM and NOA streams (Figure S4). Optimal flow rates were selected to achieve maximum PCM loading while ensuring stable production of monodispersed droplets. The droplets were subsequently exposed to UV radiation in a 50 cm long polyethylene tube inside a 45 cm × 20 cm × 25 cm UV chamber. The UV polymerization was achieved "on-the-fly," facilitated by two parallel tubular UV lamps (8 W, 220 V) producing UV-A radiation. The resultant solid microcapsules were removed from the chamber exit, subjected to multiple washings to eliminate glycerol, PVA, and other impurities, and left to undergo natural drying.

2.3. Characterization of Microcapsules. Scanning electron microscopy (Jeol 7100) featured a hot Schottky field-emission gun, which was utilized to assess the morphology of microcapsules. The elemental analysis of the shell was carried out in combination with SEM, using energy-dispersive X-ray (EDX) spectroscopy. Prior to the analysis with SEM and EDX, each sample was subjected to gold-sputtering in a high vacuum environment.

The thermal energy storage effectiveness and thermal reversibility of microcapsule samples were assessed with a differential scanning calorimeter (DSC, Q20/TA Instruments) in the temperature ranges 0−30 °C and 0−30−0 °C, respectively, at a ramp rate of 5 °C/min in a nitrogen atmosphere.

The thermal stability of microcapsule samples was studied utilizing a thermogravimetric analyzer (TGA55/TA Instruments). Sample temperature was increased from 35 to 700 °C inside a platinum pan by applying a continuous ramp rate of 10 °C/min in a nitrogen environment.

The thermal reliability of the microcapsule sample was studied by observing phase transitions with the help of a polarizing microscope (Eclipse LV100ND, Nikon, Japan) equipped with a temperature-controlled stage. The polarizing microscope enabled visualization of phase transitions through color changes in the samples. Ten cycles of crystallization and melting were performed on the samples between 0 and 30 °C, with constant cooling and heating rates of 20 °C per minute. Temperature was maintained for 20 s at 30 °C and 40 s at 0 °C to allow all capsules to crystallize or melt. The duration of a single heating/cooling cycle was 240 s, and the pictures were taken on average every 2.587 s.

Magnetic properties of the microcapsules were measured using a Cryogenic Ltd. vibrating sample magnetometer (VSM) at 295 K with a field ramp rate of 0.2 T/min. The VSM uses a detection coilset that the sample is centered in and then vibrated at a reference frequency. Based on Faraday's law of induction, a voltage proportional to magnetic moment can be measured and compared to a nickel calibration standard to determine the actual magnetic moment. A small quantity of the sample powder was weighed into gelatin capsules and loaded into the instrument for measurement. Due to the low signal, the samples were visually aligned to a reference position determined using a nickel calibration sample, where the central position for the coilset was already known.

3. RESULTS AND DISCUSSION

3.1. Fabrication Strategy of Microcapsules. The Lego-inspired microfluidic device is illustrated in Figure 1a. It is made up of two round capillaries with tapered ends placed in a larger round capillary such that their tips face each other. The large capillary inner diameter (1.56 mm) is bigger than the

inner capillary outer diameter (1.05 mm), providing an annular gap for introducing the middle and outer fluids. Traditionally, the inner round capillary was supported by an outer square capillary,[26] but the Lego device enables the capillaries to be independently supported, and therefore, a round capillary can be placed inside a larger round capillary. Notably, leaks from capillaries are prevented by a combination of screws, O-rings, and fasteners. This glue-free design allows for the reusability of capillaries and reduces setup time from several hours to just a few minutes. Operation of the device involves injecting the inner phase (PCM) via the left injection capillary, delivering the middle phase (a dispersion of Fe_3O_4 nanoparticles in an NOA/acetone mixture) into the device through the annular space between the injection and large capillary, and supplying the outer phase from the opposite side between the collection and large capillary. This flow pattern leads to the encapsulation of PCM by the NOA middle phase once it exits the injection capillary, resulting in core−shell droplets in the collection capillary, Figure 1b. The resulting droplet generation rate was typically 3370 drops/min.

3.2. Confirmation of Fe_3O_4 Nanoparticles.
Figure 2 illustrates the results of EDX analysis for samples MC4, MC5, and MC2, showcasing the elemental composition in atomic percentages across the exposed surface of an individual microcapsule. The EDX spectra identified carbon (C), oxygen (O), and sulfur (S) as the predominant elements, alongside the consistent presence of iron (Fe) across all samples. Oxygen is present in carbonyl groups of triallyl isocyanurate and ester groups of mercapto-ester, while sulfur originates from thiol groups of mercapto-ester. The proportion of Fe is higher in the samples with the higher Fe_3O_4 loading in the middle phase, confirming the successful incorporation of magnetic nanoparticles in the shell. A decline in the weight percentage of carbon (C) and sulfur (S) was observed in the samples with increasing Fe content, suggesting that Fe_3O_4 effectively covered a larger portion of the polymeric surface of the capsules, diminishing exposure of the polymer surface. It is anticipated that the presence of Fe_3O_4 on the microcapsule surface would impart a magnetic effect.

Additionally, photographs shown in Figure 2d demonstrate the uniform dispersion of magnetic microcapsules in water, forming an aqueous suspension following agitation. Importantly, these microcapsules exhibit swift magnetization upon exposure to a neodymium magnet, leading to their attraction to the glass tube wall because of a magnetic field. The aggregated microcapsules promptly redispersed upon agitation of the glass tube once the magnetic field is withdrawn. These observations confirmed that microcapsules are not prone to agglomeration in the aqueous phase in the absence of a magnetic field and exhibit rapid responsiveness to external magnetic fields, thus ensuring efficient magnetic manipulation in practical applications. Furthermore, the Keyence VHX7000 4k microscope with Z-stacking capabilities was used to obtain a 3D image of the capsule surfaces, which further confirmed the presence of the embedded nanoparticles (Figure 2e). The high magnification and resolution of this microscope allowed for the observation of surface features down to a nanometer scale. The roughness observed over the capsule surface can be attributed to the embedded Fe_3O_4 nanoparticles. These nanoparticles have a size range of 10−50 nm, and their presence on the surface creates a textured appearance.

3.3. Microcapsule Morphology Control in Microfluidics.
In this section, we aimed to investigate the influence
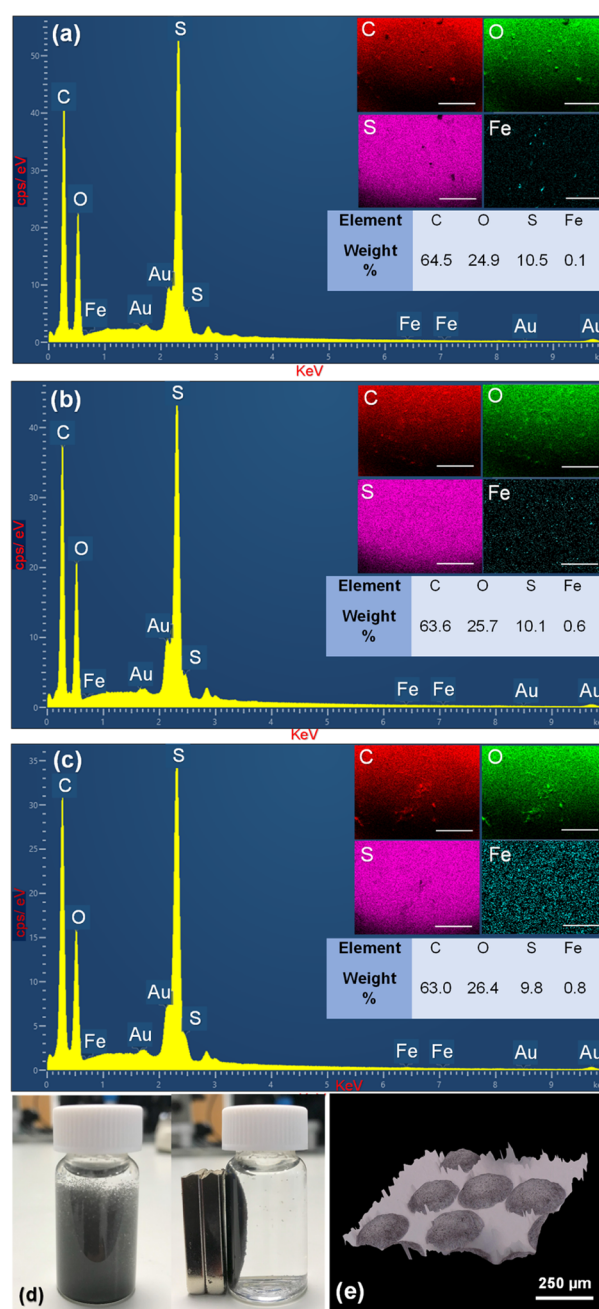
Figure 2. EDX spectra and elemental mappings obtained by scanning single microcapsule of the samples: (a) MC4; (b) MC5; (c) MC2 (scale bars 250 μm); (d) digital photographs of the microcapsule suspension and the microcapsules attracted by a magnet; (e) 3D image of microcapsules showing Fe_3O_4 nanoparticles embedded over the surface.

of inner fluid flow rate (Q_i) on the morphology of microcapsules. For this purpose, capsules were generated by varying Q_i from 0.5 mL/h (MC4) to 1.0 mL/h (MC2) to 2 mL/h (MC5), maintaining the middle phase flow rate (Q_m) at 1.0 mL/h, outer phase flow rate (Q_o) at 20 mL/h, and the inner diameters of the entry section of the injection and collection tube (D_{ii} and D_{ci}) at 100 and 400 μm, respectively. The resultant droplets and microcapsules are presented in Figure 3 and Movie S1. The bright-field micrographs in Figure 3 demonstrated a high size uniformity of microcapsules in all samples. Moreover, Fe_3O_4 nanoparticles are clearly visible,
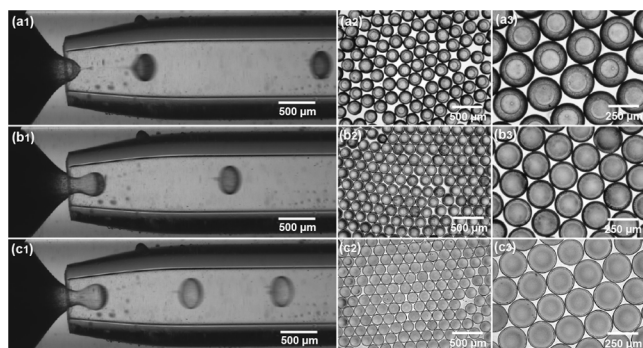
Figure 3. Microfluidic generation of core–shell droplets with varied shell thicknesses for samples: (a1) MC1; (b1) MC2; (c1) MC3. (a2), (b2), (c2) and (a3), (b3), (c3) are the corresponding bright-field microscopy images of consolidated microcapsules, captured at magnifications of 4× and 10×, respectively.

confirming their incorporation in the polymer shell. The middle fluid stream in the device in Figure 3a1, b1, and c1 is black and nontransparent due to the presence of suspended Fe_3O_4 nanoparticles. Consequently, the injection capillary is not visible in the figures.

The particle size uniformity was assessed by determining the coefficient of variation (CV) for Figure 3a2, b2, and c2 using the formula: CV = σ/D, where σ represents the standard deviation (SD) of particle sizes, and D is the average particle diameter (Figure S5). The average particle diameters in Figure 3a2, b2, and c2 are 259 ± 9.24 μm, 222 ± 6.62 μm, and 222 ± 4.96 μm, with corresponding CVs of 3.3%, 3.0%, and 2.6%, respectively. Given that the CV values are close to 3%, which is widely regarded as the upper limit for highly monodisperse particles, it can be confirmed that the particles are indeed monodisperse.

The investigation of microcapsule surface morphology and the measurement of shell thicknesses were carried out using SEM analysis. Observation of surface morphology is essential in assessing the quality of PCM microcapsules, given its close correlation with attributes such as dispersibility, flowability, adherence behavior, and attrition resistance of particles. This was carried out through SEM images depicted in Figure 4,
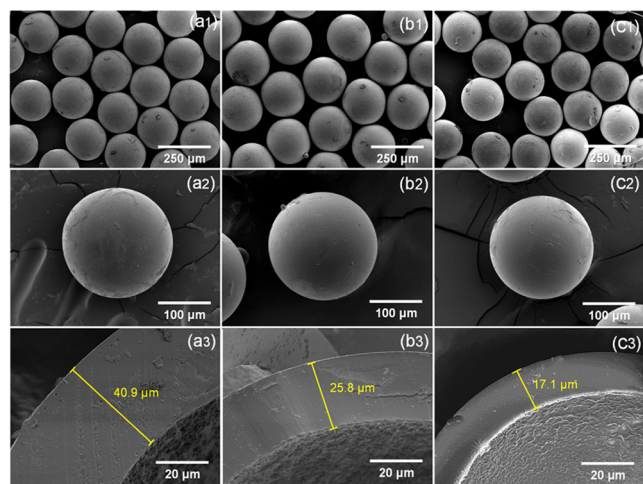
Figure 4. SEM images of microcapsules: (a1, a2) MC1; (b1, b2) MC2; (c1, c2) MC3. (a3), (b3), and (c3) Shell thicknesses of the corresponding samples measured after microtome cutting.

which illustrate a consistent spherical configuration of microcapsules specified by a notably narrow particle size distribution and the absence of polymer bridges between particles. This outcome is ascribed to the meticulous emulsification procedure followed by quick polymerization, underscoring their robust formation. Upon closer examination of SEM images in Figure 4a2, b2, and c2, it becomes apparent that the microcapsules manifest smooth and compact surfaces without any irregularities such as dimples, despite the application of substantial vacuum conditions during the sample preparation phase.

Subsequently, we aimed to investigate how the microcapsule shell thickness was affected by PCM flow rate. Increasing the shell thickness is an easy way for increasing the thermal and mechanical robustnesses of microcapsules and their magnetic responsiveness. Indeed, thin shells are susceptible to rupture when subjected to mechanical or thermal stresses, potentially leading to PCM leakage and reduced product longevity.[27] Nevertheless, the microcapsule capacity to load PCM and store heat is reduced when the shell thickness is beyond an optimal value. The mass balance equation associated with droplet formation can be used to anticipate the shell thickness of core–shell droplets (δ_d). If there is no mass transfer between the liquid streams during droplet formation:

$$\delta_d = \frac{d_o}{2}\left[1 - \left(1 + \frac{Q_m}{Q_i}\right)^{-1/3}\right]$$

(1)

At constant orifice size, the outer diameter of core–shell droplets (d_o) primarily depends on the shear stress imposed by the outer phase, which depends on Q_o and Q_m. Thus, at constant Q_m and Q_o, the shell thickness is modulated by Q_i, wherein greater Q_i values result in thinner shells following eq 1.

In Figure 4a3, b3, and c3, the ratio of middle fluid to inner fluid flow rates (Q_m/Q_i) is decreased from 2.0 to 1.0 to 0.5, and microcapsule shell thickness decreases from 40.9 to 25.8 to 17.1 μm, matching the values anticipated by the mass balance of the microfluidic process. The minimum observed shell thickness of 17.1 μm (Figure 4c3) was attained at the largest inner phase flow rate of 2 mL/h. By increasing the acetone content within the NOA phase and additionally increasing the inner phase flow rate, the shell thickness could be further decreased to levels below 17 μm, consequently enhancing PCM loading. However, further research is necessary to confirm this relationship, optimize the process, and explore more sustainable options for solvent selection. A dense and compact polymeric shell was visible upon examination of the microcapsule cross sections in Figure 4a3, b3, and c3. This signifies that porosity or structural inhomogeneities in the NOA shell was not caused by acetone evaporating from the middle phase. Movie S1 depicts how shell thickness relies on the flow rate of the inner phase. The underlying mass balance equations of the process also provide an understanding of this correlation. The volume fraction of acetone within the NOA phase is

$$v_a = \frac{\rho_m}{\rho_a}x_a$$

(2)

where ρ_m and ρ_a represent the densities of NOA/acetone mixture (middle phase) and pure acetone, respectively, and x_a denotes the acetone weight fraction. Due to the small content of Fe_3O_4 nanoparticles, their presence in the shell was

neglected. The volume fraction of HD inside microcapsules can be written as

$$\frac{Q_i}{Q_i + Q_m(1 - v_a)} = \left(\frac{d_i}{D_2}\right)^3 \qquad (3)$$

where Q_i is the volumetric flow rate of the inner phase (core material), $Q_m(1 - v_a)$ is the volumetric flow rate of the shell-forming material (pure NOA), and D_2 is the outer diameter of microcapsules. From eqs 2 and 3, the core diameter (d_i) of microcapsules will be

$$d_i = D_2 \left[\frac{Q_i}{Q_i + Q_m(1 - v_a)}\right]^{1/3} \qquad (4)$$

The shell thickness of microcapsules (δ_c) can then be computed using the equation:

$$\delta_c = \frac{D_2 - d_i}{2} = \frac{D_2}{2}\left\{1 - \left[\frac{Q_i}{Q_i + Q_m(1 - v_a)}\right]^{1/3}\right\} \qquad (5)$$

Based on $\rho_m = 1.07$ g/cm^3, $\rho_a = 0.785$ g/cm^3, $x_a = 0.2$, and $v_a = 0.28$, the shell thicknesses of MC1, MC2, and MC3 calculated using eq 5 are 40.1 μm, 25.2 μm, and 17.5 μm, respectively. These values are in good accordance with measurements taken through SEM images of microcapsule cross sections, confirming the complete encapsulation of HD inside microcapsules. Thus, the mass balance equations presented in this study can be employed to estimate the necessary flow rates for precise control of HD microcapsule thickness.[25]

3.4. Energy Storage Performance of Microcapsules.
An efficient PCM necessitates a substantial melting enthalpy. The above mass balance equations can be used to calculate the heat storage capacity of PCM microcapsules. The theoretical PCM content (E_{theo}) of microcapsules can be predicted from the mass flow rates of HD ($\dot{m}_h = \rho_h Q_i = 0.77 Q_i$) as well as pure NOA [$\dot{m}_{NOA} = \rho_{NOA}(1 - v_a)Q_m = 1.17(1 - v_a)Q_m$], where ρ_h, ρ_a, and ρ_{NOA} represent the respective densities (g/mL) of HD, acetone, and NOA, respectively. The theoretical PCM content of microcapsules is based on the assumptions that all HD becomes encapsulated within NOA shells, and all acetone initially dissolved in NOA permeates into the outer aqueous phase and subsequently volatilizes into the surrounding air. In this case,

$$E_{theo} = \frac{0.77 Q_i}{0.77 Q_i + 1.17(1 - v_a)Q_m} \times 100\% \qquad (6)$$

DSC analysis was employed to analyze the thermal energy storage and release performance of three representative microcapsule samples alongside pure PCM. This analysis aimed to match the experimental outcomes against theoretical projections for PCM content while also enabling an accurate assessment of the thermal characteristics of microcapsules. DSC thermograms obtained are presented in Figure 5, and a comprehensive summary of the thermal properties of these samples is compiled in Table 2.

The phase change enthalpies ΔH_m and ΔH_c were determined by evaluating the areas between the peaks and the baseline during both heating and cooling phases of a DSC cycle, while the temperatures at which these phase changes occurred (T_m and T_c) were found based on the positions of
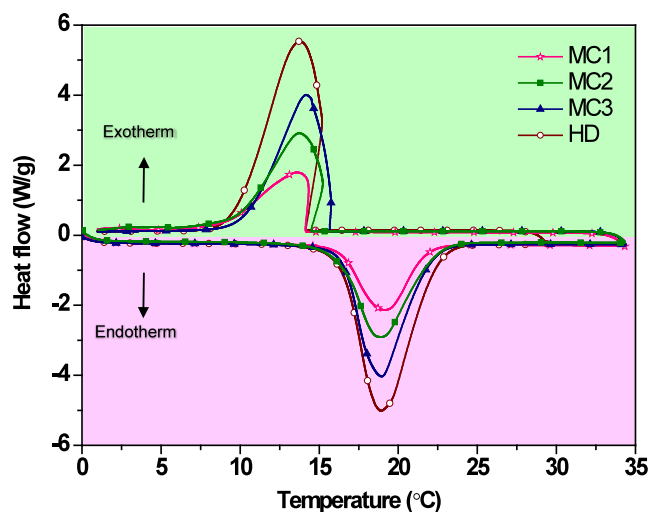
Figure 5. DSC thermograms of HD, MC1, MC2, and MC3.

Table 2. Thermal Properties of HD and Microcapsule Samples (T_m = Melting Point, T_c = Crystallization Point, ΔH_m = Latent Heat of Melting, ΔH_c = Latent Heat of Crystallization, E = PCM Content)

sample	T_m(°C)	ΔH_m (J/g)	T_c(°C)	ΔH_c (J/g)	E_{exp}(%)	E_{theo}(%)
HD	18.9	240	13.8	239	NA	NA
MC1	19.1	71	14.0	72	29.5	29.0
MC2	19.1	109	14.2	109	44.6	45.0
MC3	19.0	152	14.2	153	63.3	62.0

these peaks. The theoretical PCM loadings (E_{theo}) were computed using eq 6.[28,29] The enthalpies of pure and encapsulated PCM were used to compute the experimental PCM loading (E_{exp}) using eq 7:

$$E_{exp} (\%) = \frac{\Delta H_{m,ePCM}}{\Delta H_{m,PCM}} \times 100 \qquad (7)$$

where $\Delta H_{m,ePCM}$ and $\Delta H_{m,PCM}$ represent melting (crystallizing) enthalpies of encapsulated and pure PCM, respectively.

In Figure 5, the thermogram of pure HD reveals an excellent melting enthalpy of 240 J/g at a temperature of 18.9 °C, thereby approving the excellent phase change characteristics of HD. The thermograms of the associated microcapsules (MC1, MC2, and MC3) exhibited phase change characteristics analogous to that of pure HD. The inherent characteristics of HD to store and release heat remain unaltered after it is encapsulated, ruling out the plausible chemical interactions between the PCM and the shell material. Additionally, the melting temperature of all microcapsule samples closely approximated the pure HD value, confirming that the heat storage characteristics originated from the HD within the microcapsule and not from the polymer shell. In comparison to the pure HD, melting temperatures of MC1, MC2, and MC3 experienced a small increase up to 0.2 °C. This increment in the melting temperatures can be attributed to the thermal resistance imparted by the shell material, which induced a shift of the melting peak toward elevated temperatures.[30] Additionally, it was observed that the freezing curves of all the samples are tilted backward. Such phenomenon can be attributed to the concurrent processes of recrystallization occurring alongside freezing. As smaller crystals form and undergo rearrangement into larger ones, heat is released. This released heat counters

Table 3. Comparison of Reported Energy Storage Performance of Microcapsules Achieved with Different Methods and Shell Materials

core	shell	nanoparticles	fabrication technique	PCM content	ref.
n-dodecane	ZrO_2	rare earth	*in situ* polycondensation	62.9	32
paraffin	SnO_2	CNT	*in situ* precipitation	42.9	33
oleic-myristic acid	MF resin	ZnO	*in situ* polymerization	53.4	34
n-eicosane	TiO_2	Fe_3O_4	sol−gel	53.5	35
n-octadecane	PMMA	TiO_2	Pickering emulsion	67.2	30
HD	PEGDA	-	traditional microfluidics	57.6	21
HD	NOA	Fe_3O_4	Lego-microfluidics	63.3	this study

the anticipated constant temperature during freezing. Furthermore, the asymmetry of the peak is because the crystallization process does not occur uniformly throughout the sample. Instead, it is likely that crystallization begins at a few nucleation sites and then propagates through the sample. This can lead to a rapid release of heat at the beginning of the crystallization process, followed by a slower release of heat as the remaining liquid crystallizes. Lastly, the supercooling phenomenon can also impact the onset of freezing temperature. Here, microscopic variations can lead to localized differences in nucleation sites and propensity for supercooling, resulting in different freezing points.[31]

The shell thickness was found to have a negligible effect on the melting temperature. However, crystallization temperatures slightly differed for pure and encapsulated PCM. Pure HD exhibited a crystallization temperature (T_c) of 13.8 °C, whereas the microencapsulated samples displayed higher T_c values (14−14.2 °C). This is attributed to the encapsulation of HD, which introduced a foreign solid surface, thereby fostering nonhomogeneous crystallization and elevating crystallization temperatures compared to pure HD. The experimental PCM loadings of MC1, MC2, and MC3 were determined as 29.5%, 44.6%, and 63.3%, respectively, while the corresponding theoretical values calculated using mass balance equations were 29%, 45%, and 62%. The rise of $\Delta H_{m,ePCM}$ for the samples produced at elevated Q_i/Q_m ratios can be ascribed to an increased quantity of injected PCM per polymer. The remarkable resemblance between the E_{exp} and E_{theo} values signify that the PCM has been completely encapsulated within the microcapsules and has not leaked or evaporated. Additionally, it confirms that acetone was completely removed from the middle phase during the washing and drying steps, reducing the capsule weight and maximizing the E_{exp} value.

Table 3 compares the heat storage capability of encapsulated PCMs from this study with that of earlier works. The heat storage ability of synthesized PCM microcapsules can either be compared with or is superior to earlier published values. Hence, the developed microfluidic process is a highly effective technique for encapsulating PCMs.

3.5. Thermal Stability of Microcapsules. The maximum operational temperature of PCM microcapsules is governed by their thermal stability. Therefore, the thermal stability of microcapsules was investigated through TGA. Figure 6 illustrates the thermograms of pure HD and microcapsule samples MC1, MC2, and MC3. The degradation characteristics and ash content obtained from these thermograms have been outlined in Table 4.

In Figure 6, pure HD showcased a singular degradation step within a temperature range of 115−166 °C without leaving any traces behind. This indicates the complete volatilization of the liquid HD substance. Conversely, all PCM microcapsules,
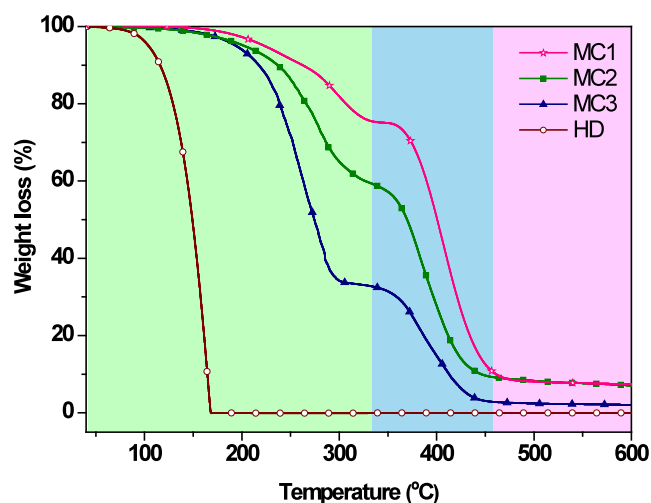
Figure 6. TGA thermograms of pure HD and microcapsule samples MC1, MC2, and MC3.

Table 4. TGA Data of HD and Different Microcapsule Samples

sample	onset (°C)	first stage		second stage		residue (%)
		T (°C)	weight loss (%)	T (°C)	weight loss (%)	
HD	115	115−166	NA	NA	NA	0.0
MC1	247	251−366	27.5	366−478	65.1	7.4
MC2	262	236−352	44.3	352−481	51.5	7.2
MC3	235	216−330	65.7	330−486	32.0	2.3

specifically MC1, MC2, and MC3, displayed a different behavior with three distinct stages of thermal degradation. The initial stage, occurring at around 236−366 °C, arises from the expansion of the polymer shell along with subsequent PCM loss due to permeation via the swollen polymer network.[36] The next stage, attributed to the melting and thermal breakdown of the NOA shell through pyrolysis, occurred at ∼330−486 °C.[37] Finally, the third phase was observed at 480−600 °C and was characterized by negligible weight loss. The cumulative weight loss for microcapsule samples was less than 100%, which can be attributed to the presence of polymer residue and Fe_3O_4 nanoparticles following complete degradation. The initial degradation stage showcased the weight losses of 27.5%, 44.3%, and 65.7% for MC1, MC2, and MC3, respectively. Remarkably, these figures are closely aligned with the PCM loading capacity derived from the DSC curves (refer to Table 2). The temperature at which HD evaporation began was estimated at 115 °C, assuming that moisture content was around 5% of the total capsule weight. Notably, the microcapsules exhibited higher onset degradation
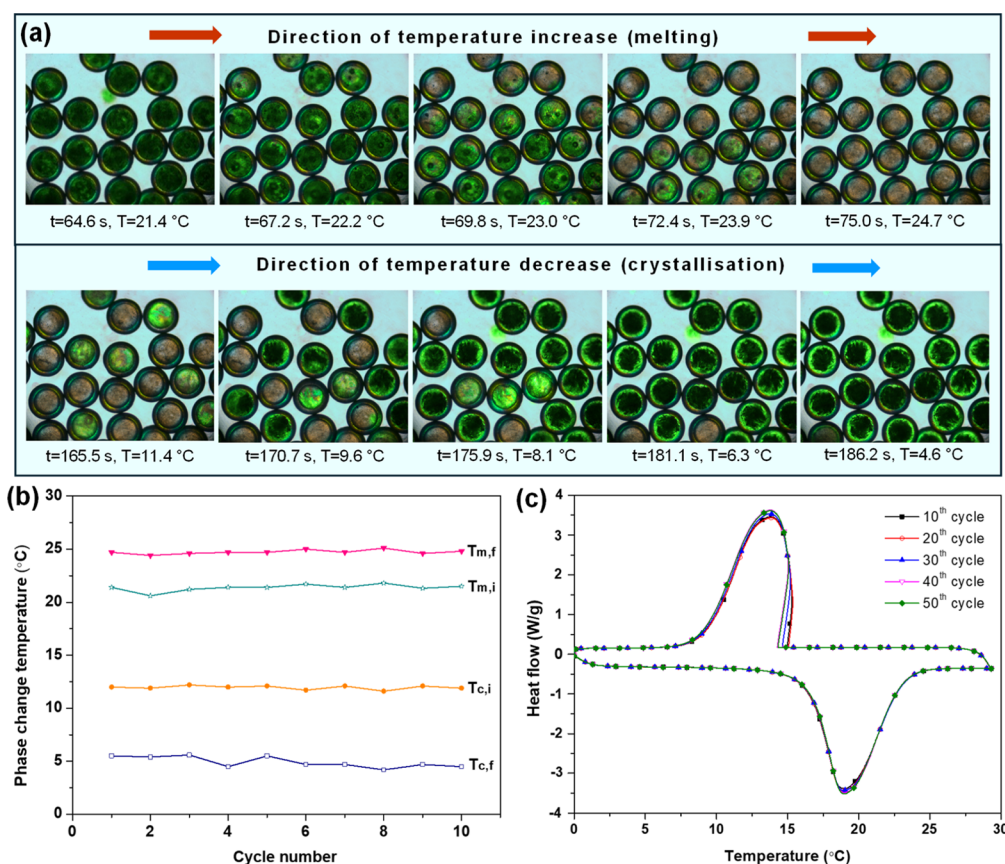
Figure 7. (a) Polarization microscopy images displaying the real-time phase change monitoring during the melting and crystallization processes of sample MC3 (a liquid HD appears light red and a crystallized HD dark green); (b) phase change parameters of microcapsule sample MC3 obtained from the thermal cycling experiment ($T_{m,i}$ is the initial melting temperature, $T_{m,f}$ the final melting temperature, $T_{c,i}$ the initial crystallization temperature, and $T_{c,f}$ the final crystallization temperature); (c) DSC thermograms of sample MC3 indicating thermal reliability.

temperatures than pure HD, underscoring their increased thermal stability. The second phase of weight reduction stemmed from the breakdown of side groups and backbone bonds in the polymer structure. By altering the ratio of inner-to-middle phase from 0.5:1 (MC1) to 2:1 (MC3), the shell thickness decreased from 40.9 to 17.1 μm, as visually depicted in Figure 4a3, b3, and c3. In comparison to MC1, reduced shell thickness of MC3 led to a decreased thermal stability. The remaining mass at 600 °C was 7.4% (MC1), 7.2% (MC2), and 2.3% (MC3), due to decreasing shell content across the respective formulations, with MC3 exhibiting the smallest residue and the smallest shell thickness.

3.6. Thermal Reliability of Microcapsules. Thermal cyclability of PCM microcapsules was studied using a real-time thermo-optical analysis by polarized light microscopy. Here, we selected the sample MC3 with highest PCM content and thinnest shell, which was prone to leak. The sample was employed on a temperature-controlled stage to experience 10 repeated melting−crystallizing cycles between temperatures 0 and 30 °C. A microscope camera equipped with polarizing filters was used for real-time monitoring of the crystallinity of the microcapsules.

Figure 7a displays a series of frames showing a gradual melting of microcapsule cores upon temperature increase from 21.3 to 24.7 °C and a gradual crystallization of microcapsule cores upon cooling from 11.4 to 4.6 °C within a single cycle. For melting, 5 consecutive time frames were selected with a time increment of 2.58 s per frame and a temperature

increment of 0.86 K per frame. For crystallization, the time increment was 5.17 s, i.e., every second frame is shown in Figure 7a. The corresponding times counted from the start of the cycle are shown for each frame. Movie S2 is a time-lapse video of all 10 heating/cooling cycles. It was observed that, although the melting temperature of HD is 18.9 °C, the melting inside the capsules started on average at 21.3 °C. The difference in temperature of 2.5 K was created due to the heat resistance of the wall and a relatively high heating rate of 20 K/min, which was 4 times faster than the cooling/heating rate in DSC analysis. The heat can only penetrate through the capsule wall if the hot stage temperature is higher than the capsule core temperature. The melting was finished within the temperature interval of 3.4 °C (from 21.3 to 24.7 °C), while the crystallization occurred within the temperature range of 6.8 °C (from 11.4 to 4.6 °C). It was because different capsules contain different amounts of micron-sized impurities suspended inside the HD core or deposited on the inner surface of shell. These impurities act as a crystallization nucleus and can trigger solidification at a higher temperature. The apparent superheating temperature was only 3.4 K, while the apparent supercooling was 6.8 K. It was hypothesized that the actual HD superheating temperature is 0 K − crystalline HD melted exactly when the temperature in the core was 18.9 °C, but due to limited heat transfer rate through the shell, the temperature in the core was 18.9 °C when temperature on the stage was already 21.4 °C. If the heating rate was infinitely small, HD in capsules would probably melt at 18.9 °C. On the other hand,

the heat resistance of the shell should be constant irrespective of the direction of heat flux. Since the apparent supercooling temperature was 6.8 K, it is assumed that the temperature difference of 3.4 K can be attributed to the heat resistance of the wall (which was the same no matter the heat flow direction), and the rest could be attributed to the actual supercooling. The reason for supercooling was the energy barrier that must be overcome in the nucleation process, which did not exist in the melting process. The energy barrier depends on the level of impurities in the capsule cores.

The phase transition temperatures at the beginning and end of each cycle exhibited remarkable consistency across different cycles with $T_{m,i}$ ranging between 21.2 and 21.8 °C, $T_{m,f}$ between 24.6 and 25.2 °C, $T_{c,i}$ between 11.0 and 11.5 °C, and $T_{c,f}$ between 4.1 and 5.3 °C (Figure 7b). All crystals were fully melted during heating part of the cycle, and no crystals were remaining from the previous cycle that could serve as nucleation sites and helped to increase the crystallization temperature in the subsequent cycle. Also, since the phase transition temperatures were highly consistent across different cycles, the thermal resistance of the shell was highly consistent, which means that the capsule shells were not damaged on repeated melting/crystallization events.

The same microcapsule sample underwent a dynamic DSC scan through 50 cycles. A series of 50 heating/cooling cycles (0−30−0 °C) was conducted, employing a ramp rate of 5 °C/min. Melting and enthalpy data were recorded at the 10th, 20th, 30th, 40th, and 50th cycles. After the first cycle, DSC thermograms aligned with those from the 50th cycle, displaying a slight ~0.4 °C variance within melting/freezing temperatures (Figure 7c). The enthalpy (melting/freezing) data fluctuation remained at approximately 1% following 50 repeated cycles.

3.7. Magnetic Properties of Microcapsules. The magnetic characteristics of the synthesized microcapsules were assessed using a VSM at a standard room temperature of 25 °C. The relevant magnetic hysteresis loops are shown in Figure 8.

Saturation magnetic induction of bare microcapsules was observed as zero, signifying the absence of any magnetic response. Conversely, when the content of Fe_3O_4 in the middle phase was 0.2 wt % (sample MC4), the measured saturation

magnetic induction was 0.024 emu/g. The saturation magnetic induction of the microcapsules exhibited a steady rise corresponding to the increase in the content of Fe_3O_4 in the middle phase. Specifically, the saturation magnetic induction for MC5 and MC3 attained the values of 0.104 and 0.194 emu/g, respectively. Superparamagnetic behavior was defined by high saturation magnetization (Ms), low remanence magnetization (Mr), and low coercive force (Hc) values, as well as the tendency of Mr/Ms to approach zero.[10,38] As depicted in Figure 8, it is evident that all magnetic microcapsules exhibited a 0 T external magnetic field, indicative of their classification as soft magnetic materials characterized by high saturation magnetic induction strength and low coercive force. This property renders the capsules readily magnetized and demagnetized (Figure 2d). Consequently, the prepared microcapsules hold significant promise for applications requiring recurrent magnetization, such as maneuverable PCMs, infrared electromagnetic dual shielding in aircraft, electronic gadgets of higher power densities, portable electronic devices, and magnetic shielding materials.

4. CONCLUSIONS

Bifunctional microcapsules composed of Fe_3O_4 nanoparticles embedded within UV-cured optical adhesive shells enclosing HD were successfully synthesized using a Lego-inspired droplet microfluidic device. The bifunctional PCM microcapsules demonstrated both magnetic properties and thermal energy storage capabilities at the same time. The existence of Fe_3O_4 nanoparticles embedded in NOA shells was confirmed using EDX and confocal microscopy. Largely monodisperse PCM microcapsules with modulated morphology, magnetic responsiveness, and heat storage capability could be readily fabricated by modifying the content of Fe_3O_4 nanoparticles in an uncured polymer phase and flow rates of all fluids within microfluidic device. The maximum PCM content achieved was 63.3%. Additionally, the accurate prediction of PCM content is achievable through the developed correlations. The melting and crystallization of microencapsulated PCM was supervised by polarized transmitted light emitted from a polarizing microscope. The capsules endured 10 repeated melting/crystallization cycles on a polarizing microscope setup with no damage to the polymer wall and without any morphological changes and any leakage of PCM. Moreover, the phase transition temperatures were highly consistent across different cycles. The sample MC3 with 1 wt % Fe_3O_4 in the uncured polymer phase exhibited the saturation magnetization of 0.194 emu/g and demonstrated high magnetic responsiveness and maneuverability. This technique can be scaled up to produce microcapsules in kilograms per hour by using multiple parallel Lego devices and/or capillaries with millimeter-sized orifice diameters. The bifunctional PCM microcapsules produced would prove beneficial as heat sinks as well as heat sources in various micro/small-scale uses such as maneuverable PCMs in micro/nanorobots, infrared electromagnetic dual shields in aircraft, and on-chip coolant for integrating circuits in electronic gadgets and portable electronic devices.

Figure 8. Magnetic hysteresis loops of bare microcapsules, MC3, MC4, and MC5.

■ ASSOCIATED CONTENT

Ⓢ Supporting Information

The Supporting Information is available free of charge at https://pubs.acs.org/doi/10.1021/acssuschemeng.4c00585.

Engineering drawing of Lego block (Figure S1); dismantled Lego-microfluidic device (Figure S2); microfluidic setup for PCM microencapsulation (Figure S3); internal geometry of capillaries in the Lego device with all notations (Figure S4); size distribution histograms of microcapsules (Figure S5) (PDF)

Droplets formation with controlled inner phase flow rate using the Lego device (Movie S1) (AVI)

Polarization microscopy movie showing 10 representative cycles of phase change of sample MC3 (Movie S2) (MP4)

■ AUTHOR INFORMATION

Corresponding Author

    Goran T. Vladisavljević − *Department of Chemical Engineering, Loughborough University, Loughborough LE11 3TU, United Kingdom;* ● orcid.org/0000-0002-8894-975X; Email: G.Vladisavljevic@lboro.ac.uk

Authors

    Sumit Parvate − *Department of Chemical Engineering, Loughborough University, Loughborough LE11 3TU, United Kingdom; Polymer and Process Engineering, Indian Institute of Technology, Saharanpur 247001, India;* ● orcid.org/0000-0003-0275-1847

    Seyedarash Moshtaghibana − *Department of Chemical Engineering, Loughborough University, Loughborough LE11 3TU, United Kingdom*

    Madhav Solanke − *Polymer and Process Engineering, Indian Institute of Technology, Saharanpur 247001, India*

    Nibina Nizar − *Department of Chemical Engineering, Loughborough University, Loughborough LE11 3TU, United Kingdom*

    Nico Leister − *Institute of Process Engineering in Life Sciences, Karlsruhe Institute of Technology, Karlsruhe 76131, Germany;* ● orcid.org/0000-0002-5318-3416

    Philipp Schochat − *Institute of Process Engineering in Life Sciences, Karlsruhe Institute of Technology, Karlsruhe 76131, Germany*

    Kelly Morrison − *Department of Physics, Loughborough University, Loughborough LE11 3TU, United Kingdom*

    Sujay Chattopadhyay − *Polymer and Process Engineering, Indian Institute of Technology, Saharanpur 247001, India;* ● orcid.org/0000-0002-3522-3031

Complete contact information is available at:
https://pubs.acs.org/10.1021/acssuschemeng.4c00585

Notes

The authors declare no competing financial interest.

■ ACKNOWLEDGMENTS

■ REFERENCES

(1) Matuszek, K.; Kar, M.; Pringle, J. M.; Macfarlane, D. R. Phase Change Materials for Renewable Energy Storage at Intermediate Temperatures. *Chem. Rev.* 2023, 123, 491−514.

(2) Zhang, B.; Zhang, Z.; Kapar, S.; Ataeian, P.; Da Silva Bernardes, J.; Berry, R.; Zhao, W.; Zhou, G.; Tam, K. C. Microencapsulation of Phase Change Materials with Polystyrene/Cellulose Nanocrystal Hybrid Shell via Pickering Emulsion Polymerization. *ACS Sustainable Chem. Eng.* 2019, 7, 17756−17767.

(3) Peng, H.; Zhang, D.; Ling, X.; Li, Y.; Wang, Y.; Yu, Q.; She, X.; Li, Y.; Ding, Y. N -Alkanes Phase Change Materials and Their Microencapsulation for Thermal Energy Storage: A Critical Review. *Energy Fuels* 2018, 32, 7262−7293.

(4) Niu, J.; Liu, H.; Wang, X.; Wu, D. Molecularly Imprinted Phase-Change Microcapsule System for Bifunctional Applications in Waste Heat Recovery and Targeted Pollutant Removal. *ACS Appl. Mater. Interfaces* 2019, 11, 37644−37664.

(5) Parvate, S.; Singh, J.; Reddy Vennapusa, J.; Dixit, P.; Chattopadhyay, S. Copper Nanoparticles Interlocked Phase-Change Microcapsules for Thermal Buffering in Packaging Application. *J. Ind. Eng. Chem.* 2021, 102, 69−85.

(6) Shen, H.; Cai, S.; Wang, Z.; Ge, Z.; Yang, W. Magnetically Driven Microrobots: Recent Progress and Future Development. *Mater. Des.* 2023, 227, 111735.

(7) Lu, Y.; Yu, D.; Dong, H.; Lv, J.; Wang, L.; Zhou, H.; Li, Z.; Liu, J.; He, Z. Magnetically Tightened Form-Stable Phase Change Materials with Modular Assembly and Geometric Conformality Features. *Nat. Commun.* 2022, 13, 1−12.

(8) Liu, X.; Wang, J.; Xie, H.; Guo, Z. Concurrent Magnetic and Thermal Energy Storage Using a Novel Phase-Change Micro-encapsulated-Nanoparticles Fluid. *J. Energy Storage* 2022, 56, 105973.

(9) Zhuang, X.; Zhang, Y.; Cai, C.; Zhang, J.; Zhu, Y. Design the Magnetic Microencapsulated Phase Change Materials with Poly-(MMA-MAA) @ n-Octadecane Modified by Fe_3O_4. *Sci. Rep.* 2018, 8, 1−11.

(10) Jiang, F.; Wang, X.; Wu, D. Magnetic Microencapsulated Phase Change Materials with an Organo-Silica Shell: Design, Synthesis and Application for Electromagnetic Shielding and Thermal Regulating Polyimide Films. *Energy* 2016, 98, 225−239.

(11) Chen, X.; Tang, Z.; Liu, P.; Gao, H.; Chang, Y.; Wang, G. Smart Utilization of Multifunctional Metal Oxides in Phase Change Materials. *Matter* 2020, 3, 708−741.

(12) Parvate, S.; Chattopadhyay, S. Complex Polymeric Micro-structures with Programmable Architecture via Pickering Emulsion-Templated In Situ Polymerization. *Langmuir* 2022, 38, 1406−1421.

(13) Yoo, Y.; Martinez, C.; Youngblood, J. P. Synthesis and Characterization of Microencapsulated Phase Change Materials with Poly(Urea-Urethane) Shells Containing Cellulose Nanocrystals. *ACS Appl. Mater. Interfaces* 2017, 9, 31763−31776.

(14) Zhang, Y.; Zheng, X.; Wang, H.; Du, Q. Encapsulated Phase Change Materials Stabilized by Modified Graphene Oxide. *J. Mater. Chem. A* 2014, 2, 5304−5314.

(15) Sun, N.; Xiao, Z. Synthesis and Performances of Phase Change Materials Microcapsules with a Polymer/BN/TiO_2 Hybrid Shell for Thermal Energy Storage. *Energy Fuels* 2017, 31, 10186−10195.

(16) Liu, H.; Wang, X.; Wu, D. Fabrication of Graphene/TiO_2/Paraffin Composite Phase Change Materials for Enhancement of Solar Energy Efficiency in Photocatalysis and Latent Heat Storage. *ACS Sustainable Chem. Eng.* 2017, 5, 4906−4915.

(17) Utada, A. S.; Lorenceau, E.; Link, D. R.; Kaplan, P. D.; Stone, H. A.; Weitz, D. A. Monodisperse Double Emulsions Generated from a Microcapillary Device. *Science* 2005, 308, 537−541.

(18) Lone, S.; Lee, H. M.; Kim, G. M.; Koh, W. G.; Cheong, I. W. Facile and Highly Efficient Microencapsulation of a Phase Change Material Using Tubular Microfluidics. *Colloids Surf., A* 2013, 422, 61−67.

(19) Fu, Z.; Su, L.; Li, J.; Yang, R.; Zhang, Z.; Liu, M.; Li, J.; Li, B. Elastic Silicone Encapsulation of N-Hexadecyl Bromide by Micro-fluidic Approach as Novel Microencapsulated Phase Change Materials. *Thermochim. Acta* 2014, 590, 24−29.

(20) Guo, Y.; Hou, T.; Wang, J.; Yan, Y.; Li, W.; Ren, Y.; Yan, S. Phase Change Materials Meet Microfluidic Encapsulation. *Adv. Sci.* 2023, 2304580, .

(21) Han, X.; Kong, T.; Zhu, P.; Wang, L. Microfluidic Encapsulation of Phase-Change Materials for High Thermal Performance. *Langmuir* **2020**, *36*, 8165−8173.

(22) Liu, Z.; Qin, S.; Chen, X.; Chen, D.; Wang, F. PDMS-PDMS Micro Channels Filled with Phase-Change Material for Chip Cooling. *Micromachines* **2018**, *9*, 165.

(23) https://www.norlandprod.com/adhesives/NOA%2081.html (accessed 4 December 2023).

(24) Masouminia, M.; Dalnoki-Veress, K.; de Lannoy, C. F.; Zhao, B. Wettability Alteration of a Thiolene-Based Polymer (NOA81): Surface Characterization and Fabrication Techniques. *Langmuir* **2023**, *39*, 2529−2536.

(25) Parvate, S.; Vladisavljević, G. T.; Leister, N.; Spyrou, A.; Bolognesi, G.; Baiocco, D.; Zhang, Z.; Chattopadhyay, S. Lego-Inspired Glass Capillary Microfluidic Device: A Technique for Bespoke Microencapsulation of Phase Change Materials. *ACS Appl. Mater. Interfaces* **2023**, *15*, 17195−17210.

(26) Vilanova, N.; Rodríguez-Abreu, C.; Fernández-Nieves, A.; Solans, C. Fabrication of Novel Silicone Capsules with Tunable Mechanical Properties by Microfluidic Techniques. *ACS Appl. Mater. Interfaces* **2013**, *5*, 5247−5252.

(27) Su, J. F.; Wang, X. Y.; Han, S.; Zhang, X. L.; Guo, Y. D.; Wang, Y. Y.; Tan, Y. Q.; Han, N. X.; Li, W. Preparation and Physicochemical Properties of Microcapsules Containing Phase-Change Material with Graphene/Organic Hybrid Structure Shells. *J. Mater. Chem. A* **2017**, *5*, 23937−23951.

(28) Jiménez-Vázquez, M.; Ramos, F. J.; Garrido, I.; López-Pedrajas, D.; Rodríguez, J. F.; Carmona, M. Production of Thermoregulating Slurries Constituted by Nanocapsules from Melamine-Formaldehyde Containing *n*-Octadecane. *J. Energy Storage* **2022**, *51*, 104465.

(29) López-Pedrajas, D.; Borreguero, A. M.; Ramos, F. J.; Rodríguez, J. F.; Jiménez-Vázquez, M.; Carmona, M. Influence of the Dispersion Characteristics for Producing Thermoregulating Nano Phase Change Slurries. *Chem. Eng. J.* **2023**, *452*, 1−13.

(30) Li, C.; Yu, H.; Song, Y.; Liang, H.; Yan, X. Preparation and Characterization of PMMA/TiO₂ Hybrid Shell Microencapsulated PCMs for Thermal Energy Storage. *Energy* **2019**, *167*, 1031−1039.

(31) Huang, Y.; Stonehouse, A.; Abeykoon, C. Encapsulation Methods for Phase Change Materials − A Critical Review. *Int. J. Heat Mass Transfer* **2023**, *200*, 123458.

(32) Zhang, Y.; Wang, X.; Wu, D. Microencapsulation of *n*-Dodecane into Zirconia Shell Doped with Rare Earth: Design and Synthesis of Bifunctional Microcapsules for Photoluminescence Enhancement and Thermal Energy Storage. *Energy* **2016**, *97*, 113−126.

(33) Ma, X.; Liu, H.; Chen, C.; Liu, Y.; Zhang, L.; Xu, B.; Xiao, F. Synthesis of Novel Microencapsulated Phase Change Material with SnO₂/CNTs Shell for Solar Energy Storage and Photo-Thermal Conversion. *Mater. Res. Express* **2020**, *7* (1), 11513.

(34) Dhivya, S.; Hussain, S. I.; Jeya Sheela, S.; Kalaiselvam, S. Experimental Study on Microcapsules of Ag Doped ZnO Nanomaterials Enhanced Oleic-Myristic Acid Eutectic PCM for Thermal Energy Storage. *Thermochim. Acta* **2019**, *671*, 70−82.

(35) Jiang, B.; Wang, X.; Wu, D. Fabrication of Microencapsulated Phase Change Materials with TiO₂/Fe₃O₄ Hybrid Shell as Thermoregulatory Enzyme Carriers: A Novel Design of Applied Energy Microsystem for Bioapplications. *Appl. Energy* **2017**, *201*, 20−33.

(36) Huang, Y. T.; Zhang, H.; Wan, X. J.; Chen, D. Z.; Chen, X. F.; Ye, X.; Ouyang, X.; Qin, S. Y.; Wen, H. X.; Tang, J. N. Carbon Nanotube-Enhanced Double-Walled Phase-Change Microcapsules for Thermal Energy Storage. *J. Mater. Chem. A* **2017**, *5*, 7482−7493.

(37) Parvate, S.; Singh, J.; Dixit, P.; Vennapusa, J. R.; Maiti, T. K.; Chattopadhyay, S. Titanium Dioxide Nanoparticle-Decorated Polymer Microcapsules Enclosing Phase Change Material for Thermal Energy Storage and Photocatalysis. *ACS Appl. Polym. Mater.* **2021**, *3*, 1866−1879.

(38) Jin, L.; Han, Q.; Wang, J.; Wang, S.; Wang, H.; Cheng, X.; Du, X.; Du, Z. Fe₃O₄-Functionalized *κ*-Carrageenan/Melanin Hybrid Aerogel-Supported Form-Stable Phase-Change Composites with Excellent Solar/Magnetic-Thermal Conversion Efficiency and Enhanced Thermal Conductivity. *ACS Sustainable Chem. Eng.* **2023**, *11*, 649−659.